

# Large bulk photovoltaic effect and second-harmonic generation in few-layer pentagonal semiconductors PdS<sub>2</sub> and PdSe<sub>2</sub>

Vijay Kumar Gudelli<sup>1</sup> and Guang-Yu Guo<sup>2,1</sup>

<sup>1</sup> Physics Division, National Center for Theoretical Sciences, Taipei 10617, Taiwan

<sup>2</sup> Department of Physics and Center for Theoretical Physics, National Taiwan University, Taipei 10617, Taiwan

E-mail: gyguo@phys.ntu.edu.tw

15 June 2021

**Abstract.** Recently, atomically thin PdSe<sub>2</sub> semiconductors with rare pentagonal Se-Pd-Se monolayers were synthesized and were also found to possess superior properties such as ultrahigh air stability, tunable band gap and high carrier mobility, thus offering a new family of two-dimensional (2D) materials for exploration of 2D semiconductor physics and for applications in advanced optoelectronic and nonlinear photonic devices. In this work, we systematically study the nonlinear optical (NLO) responses [namely, bulk photovoltaic effect (BPVE), second-harmonic generation (SHG) and linear electric-optic (LEO) effect] of non-centrosymmetric bilayer (BL) and four-layer (FL) PdS<sub>2</sub> and PdSe<sub>2</sub> by applying the first-principles density functional theory with the generalized gradient approximation plus scissors-correction. First of all, we find that these few-layer PdX<sub>2</sub> (X = S and Se) exhibit prominent BPVE. In particular, the calculated shift current conductivity is in the order of 130  $\mu\text{A}/\text{V}^2$ , being very high compared to known BPVE materials. Similarly, their injection current susceptibilities are in the order of  $100 \times 10^8 \text{A}/\text{V}^2\text{s}$ , again being large. Secondly, the calculated SHG coefficients ( $\chi^{(2)}$ ) of these materials are also large, being one order higher than that of the best-known few-layer group 6B transition metal dichalcogenides. For example, the maximum magnitude of  $\chi^{(2)}$  can reach  $1.4 \times 10^3 \text{pm}/\text{V}$  for BL PdSe<sub>2</sub> at 1.9 eV and  $1.2 \times 10^3 \text{pm}/\text{V}$  at 3.1 eV for BL PdS<sub>2</sub>. Thirdly we find significant LEO coefficients for these structures in the low photon energy. All these indicate that 2D PdX<sub>2</sub> semiconductors will find promising NLO applications in light signal modulators, frequency converters, electro-optical switches and photovoltaic solar cells. Fourthly, we find that the large BPVE and SHG of the few-layer PdX<sub>2</sub> structures are due to strong intralayer directional covalent bonding and also 2D quantum confinement. Finally, we also discuss the prominent features of these NLO spectra of these materials in terms of their electronic structure and optical dielectric functions.

## 1. Introduction

Because of their extraordinary electronic and optical properties, two-dimensional (2D) materials such as graphene, atomically thin (few-layer) transition metal dichalcogenides (TMDCs) and black phosphorus, have attracted an enormous amount of interest in recent years, finding diverse applications in electronic, optoelectronic

and nonlinear photonic devices with superior performances. Among them, group 6B TMDC semiconductors with chemical formula MX<sub>2</sub> (M = Mo, W; X = S, Se) and each layer made up of a 2D hexagonal array of M atoms sandwiched between the similar arrays of X atoms, constitute a particularly interesting family of 2D materials. In particular, they were found to exhibit an indirect to direct band gap transition when they were thinned down to a monolayer (ML) [1]. This makes the MX<sub>2</sub> MLs semiconductors with a direct band gap, thus becoming promising materials for, e.g., electro-optical devices with efficient light emission [1] and field effect transistors with high on-off ratios [2]. Furthermore, these hexagonal 2D MX<sub>2</sub> materials with an odd layer-number lack the spatial inversion symmetry, although their bulk crystals are centrosymmetric. This broken inversion symmetry makes them exhibit novel properties of fundamental and technological interests, especially second-order nonlinear optical (NLO) responses such as second-harmonic generation (SHG) [3–5] and bulk photovoltaic effect (BPVE) [6].

Stimulated by the recent fabrications of few-layer PdSe<sub>2</sub> via molecular beam epitaxy, chemical vapor deposition and mechanical exfoliation [7–9], palladium-based TMDC 2D materials have also attracted much attention in the past five years [10]. Indeed, these few-layer Pd-based TMDC materials were found to exhibit some desired properties for applications, such as tunable band gap, high carrier mobility, anisotropy, enhanced thermoelectric property and ultrahigh air stability [7, 10–12]. There are several distinct differences between group 6B TMDC and Pd-based TMDC 2D materials. In particular, compared with Mo and W atoms, Pd atoms have a nearly filled *d*-shell and thus there are stronger hybridization between Pd *d*-orbitals and chalcogen *p*-orbitals in Pd-based TMDC 2D materials. This result in stronger covalent bonding within each PdX<sub>2</sub> (X = S and Se) layer as well as stronger interlayer binding. The latter gives rise to layer-number dependent properties especially band gap size [7, 10]. In contrast to groups 5B and 6B TMDCs, bulk PdS<sub>2</sub> and PdSe<sub>2</sub> crystallize in the orthorhombic layered structure [see Fig. 1(a)] with the centrosymmetric *Pbca* space group [13, 14]. Furthermore, in each PdX<sub>2</sub> layer, a Pd atom bonds with four chalcogen atoms, and Pd and chalcogen atoms form a buckled pentagonal layered structure [see Fig. 1(c)] [7, 12]. Depending on their thickness (i.e., layer-number), few-layer PdX<sub>2</sub> structures have different symmetries compared with their bulk crystals. Interestingly, 2D PdX<sub>2</sub> materials with an even layer-number crystallizes in a noncentrosymmetric structure with space group *Pca*2<sub>1</sub> and point group symmetry of *C*<sub>2v</sub> (or *mm*2), while 2D PdX<sub>2</sub> materials with an odd layer-number form a centrosymmetric structure of space group *P*2<sub>1</sub>/*c* [7, 10, 15]. Note that 2D group 6B TMDC structures with an odd-layer number are noncentrosymmetric, while that with an even layer-number have the inversion symmetry. Therefore, as for few-layer group 6B TMDC materials with an odd layer-number, 2D PdX<sub>2</sub> structures with an even layer-number are expected to show second-order NLO properties. Indeed, strong angle-dependent SHG signals in bilayer (BL) and four-layer (FL) PdSe<sub>2</sub> were observed recently [16], although the precise SHG susceptibility was not determined. Motivated by these exciting developments, in this work we perform a systematic theoretical study of the NLO responses of BL and FL PdX<sub>2</sub>, based on first-principles density functional theory (DFT) calculations.

In this paper, we focus on three principal second-order NLO responses of few-layer PdX<sub>2</sub> materials, namely, second-harmonic generation, linear electric-optical (LEO) effect and bulk photovoltaic effect. The SHG, one of the best-known second-order NLO effects, converts the two photons of the same-frequency into a new photon with

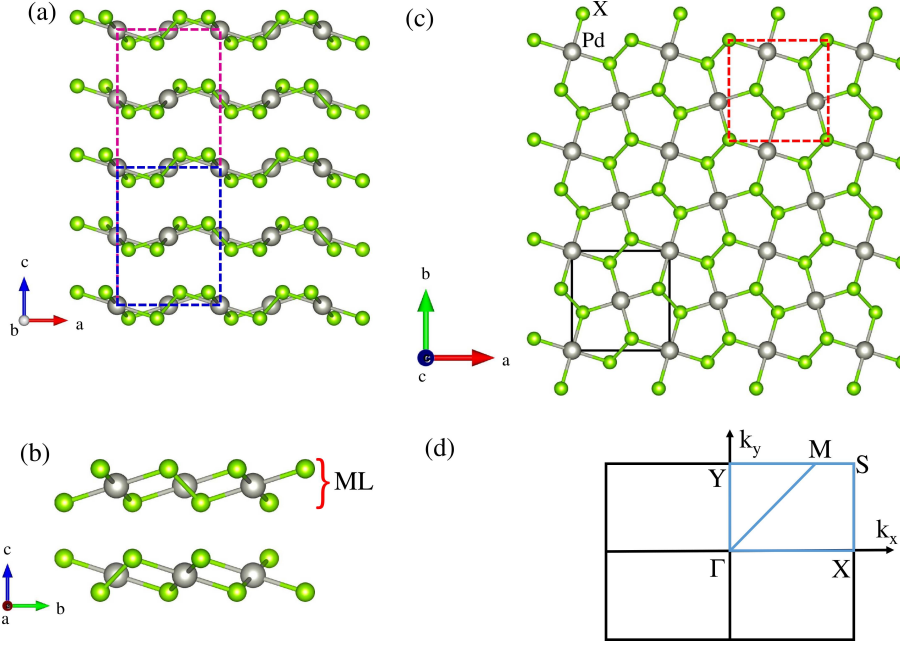


Figure 1: (a) Crystal structure of bulk  $\text{PdX}_2$  (side view along the  $b$ -axis), where blue dashed lines (magenta dashed lines) represent the unit cell of BL  $\text{PdX}_2$  (FL  $\text{PdX}_2$ ). (b) Crystal structure of BL  $\text{PdX}_2$  (side view along the  $a$ -axis). (c) Top view of the  $\text{PdX}_2$  structures. Here black solid lines (red dashed lines) show the unit cell (the pentagon) of a  $\text{PdX}_2$  layer. (d) 2D Brillouin zone (BZ) for BL and FL  $\text{PdX}_2$  structures. The blue rectangle denotes the irreducible BZ wedge. The conduction band minimum is located at a general  $k$ -point on the  $\Gamma$ -M line (see the text).

a doubled photon energy [3, 4]. Noncentrosymmetric materials with a large SHG susceptibility  $\chi^{(2)}(-2\omega; \omega, \omega)$  have many applications in nonlinear photonic devices such as frequency conversion. The SHG is also a powerful probe of the symmetry of surfaces and interfaces [3]. Here we find that all  $\text{PdX}_2$  structures possess large  $\chi^{(2)}$  in the visible frequency spectrum and BL  $\text{PdSe}_2$  has the largest  $\chi^{(2)}$  value of  $1.4 \times 10^3$  pm/V at 1.9 eV. The LEO effect refers to the linear refractive index change ( $\Delta n$ ) with the applied electric field strength ( $E$ ),  $\Delta n = n^3 r E / 2$ , where  $n$  is the refraction index and  $r$  is the LEO coefficient [4]. The LEO effect thus allows one to use an electrical signal to control the amplitude, phase or direction of a light beam in the NLO material, and leads to a widely used means for high-speed optical modulation and sensing devices (see, e.g., Ref. [17] and references therein). We find that the LEO coefficients of BL  $\text{PdS}_2$  and BL  $\text{PdSe}_2$  are significant and comparable to that of trilayer group 6B TMDC semiconductors [5]. The BPVE (also known as photogalvanic effect) refers to the generation of dc photocurrents in noncentrosymmetric materials [6]. In a nonmagnetic semiconductor, there are two main contributions to the BPVE, namely, the circular injection current and linear shift current [6, 18–20]. Materials having large BPVE are crucial for applications in photovoltaic solar cells and high sensitive photodetectors. Here we predict that the BPVE in the considered few-layer  $\text{PdX}_2$  structures is generally strong, with a large shift current conductivity of

up to 130  $\mu\text{A}/\text{V}^2$  and injection current susceptibility of up to  $100 \times 10^8 \text{ A}/\text{V}^2\text{s}$  in the visible frequency range. These superior NLO responses of the BL and FL PdX<sub>2</sub> structures will make them valuable for technological applications in NLO and electro-optic devices such as light signal modulators, frequency converters, electro-optical switches, photovoltaics and photodetector applications.

## 2. Computational methods

Bulk PdX<sub>2</sub> crystallize in a layered orthorhombic structure with space group *Pbca* (see Fig. 1), as mentioned above. The experimental lattice constants are  $a=5.460 \text{ \AA}$ ,  $b=5.541 \text{ \AA}$  and  $c=7.531 \text{ \AA}$  for PdS<sub>2</sub> [13] and  $a=5.7457 \text{ \AA}$ ,  $b=5.8679 \text{ \AA}$  and  $c=7.6976 \text{ \AA}$  for PdSe<sub>2</sub> [14]. The bulk unit cell contains two X-Pd-X monolayers stacked along the *c*-axis and each nearly squared inplane unit cell contains two chemical formulas (f.u.) (i.e., six atoms) (see Fig. 1). In each X-Pd-X layer, interestingly, a Pd atom bonds with four chalcogen atoms, and Pd and chalcogen atoms form a rare pentagonal structure [see Fig. 1(c)] [7, 12]. In the present calculations, a BL (FL) structure is constructed by cutting two (four) X-Pd-X layers out of the bulk crystal. The slab-superlattice approach is adopted with the separations of neighboring slabs being at least 15  $\text{\AA}$ . We notice that a number of the structural optimization calculations for bulk PdSe<sub>2</sub> using more than ten exchange-correlation functionals have been carried out [7, 9, 15, 21]. The discrepancies between the experimental and theoretical lattice constants are large, varying from 2 % all the way up to 20 % depending strongly on the exchange-correlation functional used [7, 21]. On the other hand, the experimental inplane lattice constants of BL PdSe<sub>2</sub> are only slightly larger than the corresponding lattice constants of bulk PdSe<sub>2</sub> [9]. Thus, we use the experimental bulk structural parameters in the present calculations. We believe that using the experimental structural parameters of atomically thin PdX<sub>2</sub> would not significantly change the calculated electronic and optical properties of BL and FL PdX<sub>2</sub> to be presented below.

The electronic structure calculations are performed using the accurate projector augmented wave method [22] as implemented in the Vienna ab-initio simulation package (VASP) [23, 24]. For the exchange-correlation potential, we adopt the generalized gradient approximation (GGA) of Perdew-Burke-Ernzerhof parametrization [25]. A large plane-wave energy cutoff of 400 eV is used throughout the calculations. The valence configuration of Pd atom is taken as  $4d^9 5s^1$ , S atom is  $3s^2 3p^4$  and for Se atom it is  $4s^2 4p^4$ . A *k*-point mesh of  $18 \times 18 \times 1$  is used in the Brillouin zone (BZ) integrations for few-layer PdX<sub>2</sub> structures. All the calculations are performed within the scalar-relativistic projector augmented potentials, with the energy convergence up to  $10^{-6}$  eV between the successive iterations.

All the linear and NLO properties of the 2D PdX<sub>2</sub> structures are calculated from the self-consistent electronic band structures within the linear response formalism with the independent-particle approximation (IPA). Specifically, we first calculate the imaginary part ( $\epsilon''(\omega)$ ) of the dielectric function due to direct interband transitions by using the Fermi golden rule [26, 27],

$$\epsilon''_a(\omega) = \frac{4\pi^2}{\Omega\omega^2} \sum_{i \in \text{VB}, j \in \text{CB}} \sum_k \omega_k |p_{ij}^a|^2 \delta(\epsilon_{\mathbf{k}j} - \epsilon_{\mathbf{k}i} - \omega) \quad (1)$$

where  $\omega$  is the photon energy and  $\Omega$  is the unit-cell volume. VB and CB denote the valence and conduction bands, respectively. The dipole transition matrix elements  $p_{ij}^a = \langle \mathbf{k}j | \hat{p}_a | \mathbf{k}i \rangle$  are obtained from the self-consistent band structures within the PAW

formalism [28]. Here  $|\mathbf{k}n\rangle$  is the  $n$ th Bloch state wave function with crystal momentum  $\mathbf{k}$ , and  $a$  denotes the Cartesian component. The obtained  $\varepsilon''(\omega)$  is used to get the real part ( $\varepsilon'(\omega)$ ) of the dielectric function by a Kramer-Kronig transformation [26, 27],

$$\varepsilon'(\omega) = 1 + \frac{2}{\pi} P \int_0^\infty \frac{\omega' \varepsilon''(\omega')}{\omega'^2 - \omega^2} d\omega', \quad (2)$$

where  $P$  is the principal value of the integral.

For the BPVE, the dc photocurrent density along the  $a$ -axis in a noncentrosymmetric material under the applied optical electric fields  $E_b$  and  $E_c$  may be written as [18, 19, 29]

$$J_a(0) = \sum_{bc} \sigma_{abc}(0; \omega, -\omega) E_b(\omega) E_c(-\omega), \quad (3)$$

where the photocurrent conductivity  $\sigma_{abc}$  is a third-rank tensor [18]. For a nonmagnetic semiconductor, the dc photocurrent contains two main contributions, namely, the linear shift current [18] and also the circular injection current [29]. That is,  $\sigma_{abc} = \sigma_{abc}^{sh} + \sigma_{abc}^{inj}$ . Within the length gauge formalism, the shift current conductivity  $\sigma_{abc}^{sh}$  can be written in terms of the interband position matrix element  $r_{ij}^a$  and its momentum derivative  $r_{ij;b}^a$  [18]. By replacing  $r_{ij}^a$  with  $p_{ij}^a/i\epsilon_{ij}$  where  $\epsilon_{ji} = (\epsilon_{\mathbf{kj}} - \epsilon_{\mathbf{ki}})$ , one may obtain

$$\sigma_{abc}^{sh}(\omega) = \frac{\pi}{\Omega} \sum_{\mathbf{k}} w_{\mathbf{k}} \sum_{i \in VB} \sum_{j \in CB} \frac{1}{\epsilon_{ij}^2} \sum_{l \neq i,j} \text{Im} \left\{ \frac{p_{il}^a \langle p_{ji}^b p_{lj}^c \rangle}{2\epsilon_{il}} + \frac{p_{lj}^a \langle p_{ji}^b p_{il}^c \rangle}{2\epsilon_{jl}} \right\} \delta(\epsilon_{ji} - \omega), \quad (4)$$

where  $\langle p_{ji}^b p_{li}^c \rangle = \frac{1}{2}(p_{ji}^b p_{li}^c + p_{li}^b p_{ji}^c)$ .

The injection current conductivity  $\sigma_{abc}^{inj} = \tau \eta_{abc}$  where  $\tau$  is the relaxation time of photoexcited carriers and  $\eta_{abc}$  is the injection current susceptibility, which can also be written in terms of  $r_{ij}^a$  and  $r_{ij;b}^a$  [see Eq. (31) in Ref. [29]]. Again, by substituting  $r_{ij}^a$  with  $p_{ij}^a/i\epsilon_{ij}$ , one would get

$$\eta_{abc}^{inj}(\omega) = \frac{2\pi}{\Omega} \sum_{\mathbf{k}} w_{\mathbf{k}} \sum_{i \in VB} \sum_{j \in CB} \frac{\Delta_{ji}^a \text{Im}[p_{ji}^b p_{ij}^c]}{\epsilon_{ij}^2} \delta(\epsilon_{ji} - \omega). \quad (5)$$

The imaginary part of the SHG susceptibility is given by [26, 30]

$$\chi_{(abc)}^{(2)}(-2\omega, \omega, \omega) = \chi_{(abc, \text{VE})}^{(2)}(-2\omega, \omega, \omega) + \chi_{(abc, \text{VH})}^{(2)}(-2\omega, \omega, \omega), \quad (6)$$

where the contribution due to the so-called virtual-electron (VE) process is [26, 30]

$$\begin{aligned} \chi_{(abc, \text{VE})}^{(2)} &= -\frac{\pi}{2\Omega} \sum_{i \in VB} \sum_{j, l \in CB} \sum_{\mathbf{k}} w_{\mathbf{k}} \left\{ \frac{\text{Im}[p_{jl}^a \langle p_{li}^b p_{ij}^c \rangle]}{\epsilon_{li}^3 (\epsilon_{li} + \epsilon_{ji})} \times \delta(\epsilon_{li} - \omega) - \frac{\text{Im}[p_{ij}^a \langle p_{jl}^b p_{li}^c \rangle]}{\epsilon_{li}^3 (2\epsilon_{li} - \epsilon_{ji})} \delta(\epsilon_{li} - \omega) \right. \\ &\quad \left. + \frac{16 \text{Im}[p_{ij}^a \langle p_{jl}^b p_{li}^c \rangle]}{\epsilon_{ji}^3 (2\epsilon_{li}^3 - \epsilon_{ji}^3)} \delta(\epsilon_{ji} - 2\omega) \right\} \end{aligned} \quad (7)$$

and that due to the virtual-hole (VH) process is [26, 30]

$$\begin{aligned} \chi_{(abc, \text{VH})}^{(2)} &= \frac{\pi}{2\Omega} \sum_{i, l \in VB} \sum_{j \in CB} \sum_{\mathbf{k}} w_{\mathbf{k}} \left\{ \frac{\text{Im}[p_{li}^a \langle p_{ij}^b p_{jl}^c \rangle]}{\epsilon_{jl}^3 (\epsilon_{jl} + \epsilon_{ji})} \times \delta(\epsilon_{jl} - \omega) - \frac{\text{Im}[p_{ij}^a \langle p_{jl}^b p_{li}^c \rangle]}{\epsilon_{jl}^3 (2\epsilon_{jl} - \epsilon_{ji})} \delta(\epsilon_{jl} - \omega) \right. \\ &\quad \left. + \frac{16 \text{Im}[p_{ij}^a \langle p_{jl}^b p_{li}^c \rangle]}{\epsilon_{ji}^3 (2\epsilon_{jl}^3 - \epsilon_{ji}^3)} \delta(\epsilon_{ji} - 2\omega) \right\}. \end{aligned} \quad (8)$$

The real part of the SHG susceptibility is then obtained from  $\chi_{abc}'^{(2)}$  by the Kramer-Kronig transformation [26, 30]:

$$\chi_{abc}'^{(2)}(-2\omega, \omega, \omega) = \frac{2}{\pi} P \int_0^\infty \frac{\omega'(\chi_{abc}''^{(2)}(2\omega', \omega', \omega'))}{\omega'^2 - \omega^2} d\omega'. \quad (9)$$

We also calculate the low-frequency LEO coefficients of the considered materials using the obtained static dielectric constants and SHG susceptibility. The LEO coefficients in the zero frequency limit are given by

$$r_{abc}(0) = -\frac{2}{\varepsilon_a(0)\varepsilon_b(0)} \lim_{\omega \rightarrow 0} \chi_{abc}''^{(2)}(-2\omega, \omega, \omega). \quad (10)$$

To ensure the accuracy of the calculated optical properties we use denser  $k$ -point meshes of  $110 \times 110 \times 1$  for BL structures and  $60 \times 60 \times 1$  for FL structures. The  $\delta$  function in Eqs. 4, 5, 7 and 8 is approximated by a Gaussian function with  $\Gamma = 0.1$  eV. Furthermore, to ensure that  $\epsilon'(\omega)$  and  $\chi'^{(2)}$  calculated via Kramer-Kronig transformation Eqs. 2 and 9 are reliable, at least 150 and 300 energy bands are included in the present optical calculations for BL and FL structures, respectively. The unit-cell volume  $\Omega$  in Eqs. 4, 5, 7 and 8 is not well-defined for low-dimensional systems. Therefore, similar to the previous calculations [5, 26, 27, 30], we use the effective unit-cell volume (i.e.,  $\Omega_{eff} = a \times b \times nd$ , where  $n$  is the layer-number and  $d$  is the effective layer thickness) of the 2D material rather than the volume of the supercell which is arbitrary. Since each unit cell of bulk PdX<sub>2</sub> contains two layers, the effective layer thickness  $d$  is 3.766 Å for few-layer PdS<sub>2</sub> and 3.849 Å for few-layer PdSe<sub>2</sub>.

Equations (1), (4), (5), (7) and (8) indicate that correct band gaps would be important for obtaining accurate optical properties. However, in general the GGA functional is known to underestimate the band gaps because some many-body effects especially the quasiparticle self-energy corrections are neglected. Therefore, we perform the band-structure calculations using the hybrid Heyd-Scuseria-Ernzerhof (HSE) functional, which is known to produce much improved band gaps for semiconductors [33, 34]. We then use the HSE band gaps and calculate all the optical properties with the well-known scissors-correction (SC) [31]. In the SC calculations, the conduction bands are uniformly up-shifted so that the band gap would match the HSE gap together with the renormalized transition matrix elements [31]. All the optical properties presented in this paper are obtained with this SC scheme.

### 3. Results and discussion

#### 3.1. Electronic structure

The calculated GGA band structures of BL PdX<sub>2</sub> and FL PdX<sub>2</sub> are presented, respectively, in Fig. 2 and Fig. S1 of the supplementary information (SI). All the four structures are an indirect band gap semiconductor. The valence band maximum (VBM) is located at the  $\Gamma$  point and the conduction band minimum (CBM) is located on the M- $\Gamma$  line in the 2D Brillouin zone [see Fig. 1(d)] for both BL and FL PdS<sub>2</sub> structures [Fig. 2(a) and Fig. S1(a)]. In the PdSe<sub>2</sub> structures, the VBM is located in the  $\Gamma$ -X direction and the CBM is located on the M- $\Gamma$  line [Fig. 2(b) and Fig. S1(b)]. The present band structure of BL PdSe<sub>2</sub> agrees rather well with that reported in Refs. [7, 9, 15]. The calculated band gaps of all the structures are listed in Table 1, together with the available experimental band gaps for BL and FL PdSe<sub>2</sub> [7, 9]. Table

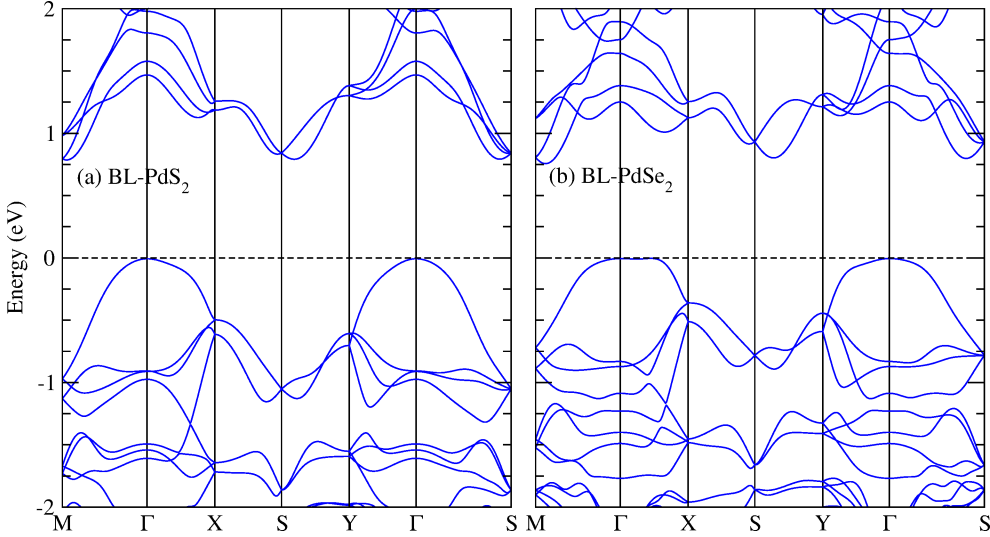


Figure 2: Band structures of (a) BL  $\text{PdS}_2$  and (b) BL  $\text{PdSe}_2$ . The horizontal dashed line denotes the top of valance bands.

1 shows that the band gap decreases significantly as the S atoms are replaced by the Se atoms in  $\text{PdX}_2$  and also as we move from the BL to FL  $\text{PdX}_2$  structure, indicating the tunability of the band gap by chalcogen substitution and also by layer-number variation.

The calculated total- and orbital-projected density of states (DOS) for BL  $\text{PdX}_2$  and FL  $\text{PdX}_2$  are presented in Fig. 3 and in Fig. S3 of the SI, respectively. Figure 3 shows that the upper valence band edge and lower conduction band edge are contributed almost equally by the Pd  $d$  orbitals and chalcogen (X)  $p$  orbitals [see Figs. 3(a) and 3(b)]. This indicates a strong covalent bonding in the  $\text{PdX}_2$  structures (see also [32]), being in rather strong contrast to group 6B TMDCs (e.g.,  $\text{MoS}_2$ ) which may be called charge-transfer semiconductors [5]. This is due to the nearly filled Pd  $d$  states in the  $\text{PdX}_2$  structures while in  $\text{MoS}_2$  the Mo  $d$  states are less than half-filled [5]. Furthermore, orbital-projected DOS spectra show that the contribution at the upper valence band edge comes predominantly from Pd  $d_{z^2}$  and chalcogen  $p_z$  with minor contribution from  $p_{x,y}$  states while the contribution at the lower conduction band edge comes from Pd  $d_{xy, x^2-y^2}$  and chalcogen  $p_{x,y}$  and  $p_z$  states. Thus, the optical transitions in  $\text{PdX}_2$  take place from the valence states of the hybridized Pd  $d$  and chalcogen  $p$  states to the conduction band states of Pd  $d$  orbitals.

Table 1 shows that the GGA band gaps for BL and FL  $\text{PdSe}_2$  are significantly smaller than the corresponding experimental values [7, 9], indicating that the GGA functional generally underestimates the band gaps of semiconductors, as mentioned in the preceding section. Therefore, we also perform the band-structure calculations using the HSE functional [33, 34] and the HSE band structures are presented in Fig S2 in the SI. Although the dispersions of the HSE band structures are similar to that of the corresponding GGA band structures, the band gaps from the HSE functional are significantly larger than that of the GGA ones (Table 1). Furthermore, the HSE band gaps of BL and FL  $\text{PdSe}_2$  are in better agreement with the experimental values

than the GGA band gaps (Table 1). Therefore, all the optical properties presented in the following sections are calculated within the scissors-correction scheme [31] by using the HSE band gaps (Table 1).

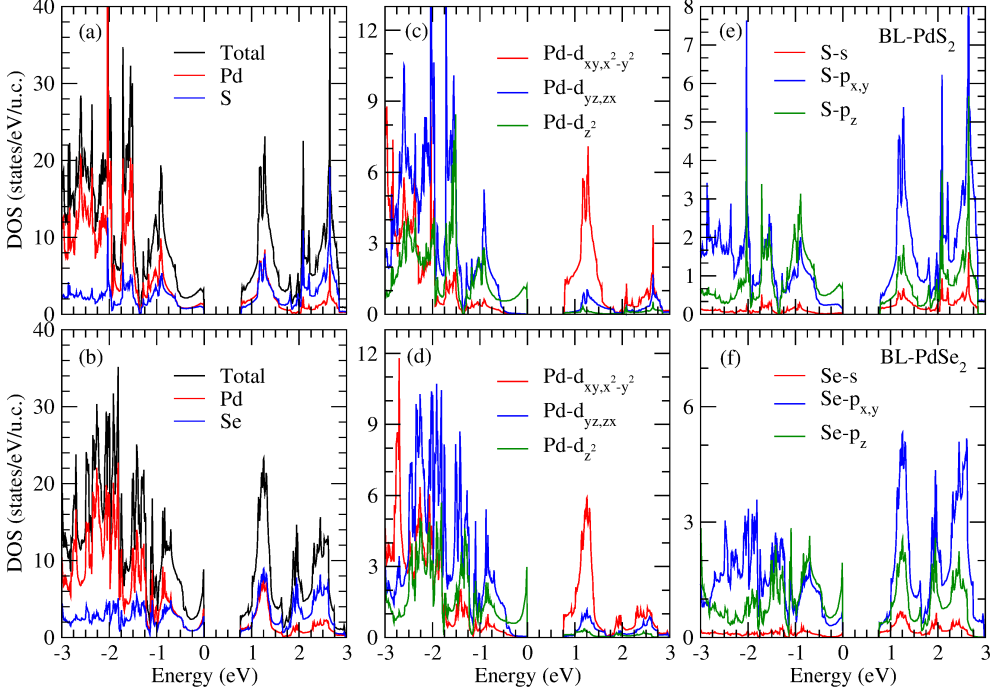


Figure 3: Total- and orbital-projected densities of states (DOS) of BL  $\text{PdS}_2$  (upper panels) and BL  $\text{PdSe}_2$  (lower panels).

Table 1: Band gaps (in eV) of BL and FL  $\text{PdX}_2$  calculated with GGA and HSE functional. The available experimental band gap values are in parentheses for comparison.

	$\text{PdS}_2$		$\text{PdSe}_2$	
	GGA	HSE	GGA	HSE
BL	0.78	1.90	0.74	1.62 (1.15 [9])
$\Delta E = E_{\text{HSE}} - E_{\text{GGA}}$		1.12		0.88
FL	0.40	1.47	0.27	1.11 (1.06 [7])
$\Delta E = E_{\text{HSE}} - E_{\text{GGA}}$		1.07		0.84

### 3.2. Linear optical properties

The calculated dielectric functions of all the four  $\text{PdX}_2$  structures are plotted in Fig. 4. As can be expected of a 2D material, there are huge differences between the out-of-plane and in-plane components of the dielectric functions (see Fig. 4). For

example, the real part of the  $z$ -polarized dielectric function  $\varepsilon'_{zz}$  is only about half of that for the in-plane polarized dielectric function  $\varepsilon'_{xx}$  and  $\varepsilon'_{yy}$  below 3 eV. The imaginary part of the  $z$ -polarized dielectric function  $\varepsilon''_{zz}$  is about four times smaller than that of the in-plane dielectric functions  $\varepsilon''_{xx}$  and  $\varepsilon''_{yy}$ . There are also discernable differences between the two in-plane components of the dielectric functions, namely,  $\varepsilon_{xx}$  and  $\varepsilon_{yy}$  (see Fig. 4). In particular, the real dielectric constant of  $\varepsilon'_{xx}$  is slightly higher than  $\varepsilon'_{yy}$  in the energy range of 2.5-3.0 (2.0-2.5) eV and 4.3-5.6 (4.0-5.0) eV, whereas  $\varepsilon'_{yy}$  in the energy range of 3.0-4.3 (2.5-4.0) eV and also in 5.6-6.0 (5.0-5.7) eV is higher than  $\varepsilon'_{xx}$  for BL PdS<sub>2</sub> (PdSe<sub>2</sub>) (see Fig. 4(a) and (c)). In FL PdS<sub>2</sub> (PdSe<sub>2</sub>) structure, the real dielectric constant  $\varepsilon'_{xx}$  is higher than  $\varepsilon'_{yy}$  in the energy range of 2.2-2.7 (1.9-2.5) eV and 4.3-5.6 (4.0-5.6) eV, whereas  $\varepsilon'_{yy}$  in the energy range of 2.7-4.3 (2.5-4.0) eV and also in 5.6-6.00 (5.0-6.0) eV is slightly higher than  $\varepsilon'_{xx}$  (see Fig. 4(e) and (g)). Similar profile is found in the imaginary part of the dielectric constant, where  $\varepsilon''_{xx}$  is higher than  $\varepsilon''_{yy}$  in the energy range of 2.6-3.1 eV (2.5-3.4 eV) and 3.9-5.0 eV (5.0-6.0 eV) for BL (FL) PdS<sub>2</sub> and 2.2-2.9 eV (2.1-3.0 eV) and 4.5-5.4 eV (4.5-5.3 eV) for BL (FL) PdSe<sub>2</sub>, whereas in the other energy windows  $\varepsilon''_{yy}$  is higher than  $\varepsilon''_{xx}$  for both BL (FL) PdS<sub>2</sub> and PdSe<sub>2</sub> structures, see Fig. 4(b) and (d) (Fig. 4(f) and (h)). It is worth mentioning that the large imaginary part of the dielectric function of all the PdX<sub>2</sub> structures spans over a wide range of the visible frequency range, which is similar to that of silicon [35]. This suggests that as for silicon, these 2D PdX<sub>2</sub> structures will be useful for opto-electronic applications such as high solar-absorption efficiency solar cells [36].

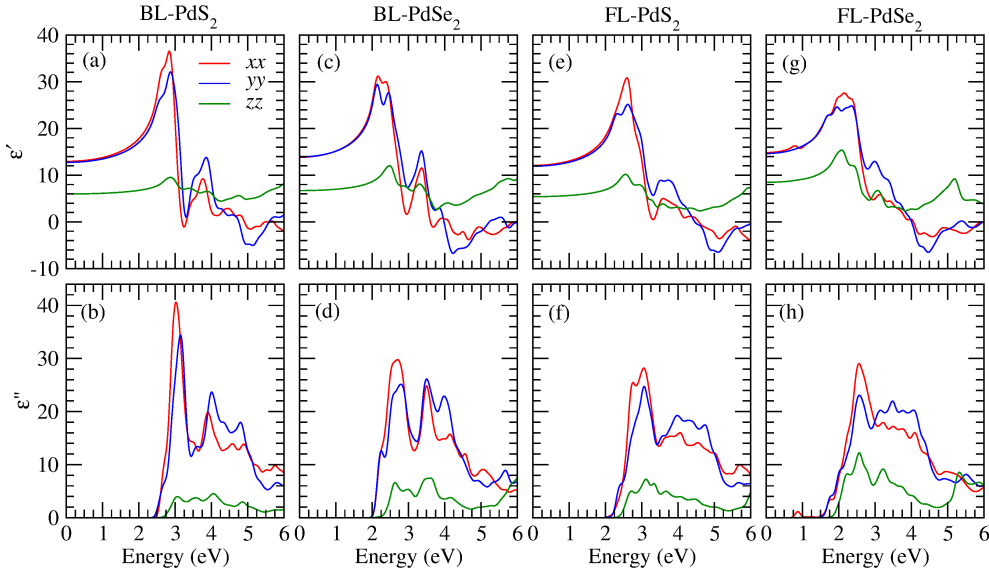


Figure 4: Real (upper panels) and imaginary (lower panels) parts of the dielectric functions of BL-PdS<sub>2</sub>, BL-PdSe<sub>2</sub>, FL-PdS<sub>2</sub>, and FL-PdSe<sub>2</sub>.

### 3.3. Shift and injection currents

As mentioned before, the point symmetry group of BL and FL PdX<sub>2</sub> is  $C_{2v}$  with the  $C_2$  rotation axis along the  $y$ -axis. Therefore, there are only five inequivalent nonzero shift current tensor elements [37], namely,  $\sigma_{xxy}^{sh} = \sigma_{xyx}^{sh}$ ,  $\sigma_{yxx}^{sh}$ ,  $\sigma_{yyy}^{sh}$ ,  $\sigma_{yzz}^{sh}$  and  $\sigma_{zyz}^{sh} = \sigma_{zzy}^{sh}$ . Similarly, there are only two inequivalent nonzero injection current susceptibility elements, namely,  $\eta_{xxy} = -\eta_{xyx}$  and  $\eta_{zzy} = -\eta_{zyz}$  [37]. Since the photocurrent cannot flow along the out-of-plane direction (the  $z$ -axis), we will not consider the nonzero elements of  $\sigma_{zyz}^{sh} = \sigma_{zzy}^{sh}$  and  $\eta_{zzy} = -\eta_{zyz}$  in the rest of this paper.

The calculated four inequivalent nonzero shift current conductivity elements for BL and FL PdX<sub>2</sub> are plotted in Fig. 5. Figure 5 shows that in all the PdX<sub>2</sub> structures, the four shift current conductivity elements are zero below the band gap but increase rapidly above the band gap. Notably, the  $\sigma_{xxy}^{sh}$  element in BL PdS<sub>2</sub> dominates the low photon energy range of 2.4~3.2 eV with a prominent peak of height of 160  $\mu\text{A}/\text{V}^2$  at 2.9 eV. The  $\sigma_{xxy}^{sh}$  of BL PdS<sub>2</sub> has a second peak with the reduced maximum of 65  $\mu\text{A}/\text{V}^2$  at 3.9 eV [see Fig. 5(a)]. For BL PdSe<sub>2</sub>, these two prominent peaks in the  $\sigma_{xxy}^{sh}$  spectrum become comparable with the maximum values of  $\sim 115$   $\mu\text{A}/\text{V}^2$  and  $\sim 126$   $\mu\text{A}/\text{V}^2$  at 2.6 eV and 3.6 eV, respectively [see Fig. 5(b)]. In both BL structures, the magnitudes of the  $\sigma_{yxx}^{sh}$  and  $\sigma_{yyy}^{sh}$  spectra are also pronounced in the photon energy range from the absorption edge to  $\sim 5.0$  eV. For example, the  $\sigma_{yyy}^{sh}$  of BL PdS<sub>2</sub> has a negative peak at  $\sim 3.9$  eV with the maximum value of -90  $\mu\text{A}/\text{V}^2$ . Fig. 5 also indicates that the magnitude of the  $\sigma_{yzz}^{sh}$  spectra from all the four structures is much smaller than all the other shift conductivity elements. This may be attributed to the fact that the absorptive part of the out-of-plane polarized dielectric function element  $\varepsilon_{zz}$  is much smaller than that of the in-plane polarized dielectric function elements  $\varepsilon_{xx}$  and  $\varepsilon_{yy}$  (see Fig. 4). In the FL structure, the maximum shift current conductivity is from  $\sigma_{xxy}^{sh}$  ( $\sigma_{yyy}^{sh}$ ) of the order of  $\sim 97$  ( $\sim 90$ )  $\mu\text{A}/\text{V}^2$  at a photon energy of 2.9 (2.5) eV for PdS<sub>2</sub> (PdSe<sub>2</sub>) [see Fig. 5(c) and (d), respectively]. Similar to the BL structures, FL PdX<sub>2</sub> also have contributions of  $\sim 50$   $\mu\text{A}/\text{V}^2$  from other elements such as  $\sigma_{yyy}^{sh}$  for FL PdS<sub>2</sub> and  $\sigma_{xxy}^{sh}$ ,  $\sigma_{yxx}^{sh}$  for FL PdSe<sub>2</sub> in the energy range of 3-4 eV [see Fig. 5(c) and (d)].

The calculated nonzero injection current susceptibility element  $\eta_{xxy}$  is displayed as a function of photon energy for both BL and FL PdX<sub>2</sub> in Fig. 6. Using the typical relaxation time  $\tau = 0.04$  ps for 2D PdX<sub>2</sub> materials [11], we obtain the injection photocurrent conductivity  $\sigma_{xxy}^{inj} = \tau\eta_{xxy}$ , as shown in Fig. 6. For all the PdX<sub>2</sub> structures, both  $\eta_{xxy}$  and  $\sigma_{xxy}^{inj}$  are zero below the absorption edge but they increase rapidly above the absorption edge. In BL PdS<sub>2</sub>, the calculated injection conductivity  $\sigma_{xxy}^{inj}$  has two negative prominent peaks with the maximum values of -240 and -360  $\mu\text{A}/\text{V}^2$  at 2.7 and 4.7 eV, respectively [see Fig. 6(b)]. Similarly, in BL PdSe<sub>2</sub>, we also find two pronounced peaks with larger maximum values of -400 and -580  $\mu\text{A}/\text{V}^2$  at 3.1 and 4.0 eV, respectively [see Fig. 6(d)]. In the FL structures, the magnitudes of both  $\eta_{xxy}$  and  $\sigma_{xxy}^{inj}$  spectra are smaller compared with that from the BL structures (Fig. 6). In particular, the magnitudes of the  $\eta_{xxy}$  and  $\sigma_{xxy}^{inj}$  of FL PdSe<sub>2</sub> are generally less than half of that from BL PdSe<sub>2</sub> [see Figs. 6(c) and 6(d)]. Nonetheless, FL PdS<sub>2</sub> and FL PdSe<sub>2</sub> do have a rather pronounced peak in the  $\sigma_{xxy}^{inj}$  spectrum with the peak value being about -200  $\mu\text{A}/\text{V}^2$  at 3.1 and 2.8 eV, respectively.

Let us now compare the BPVE in the present structures with the well-known BPVE materials to access their application potentials in photovoltaic solar cells and

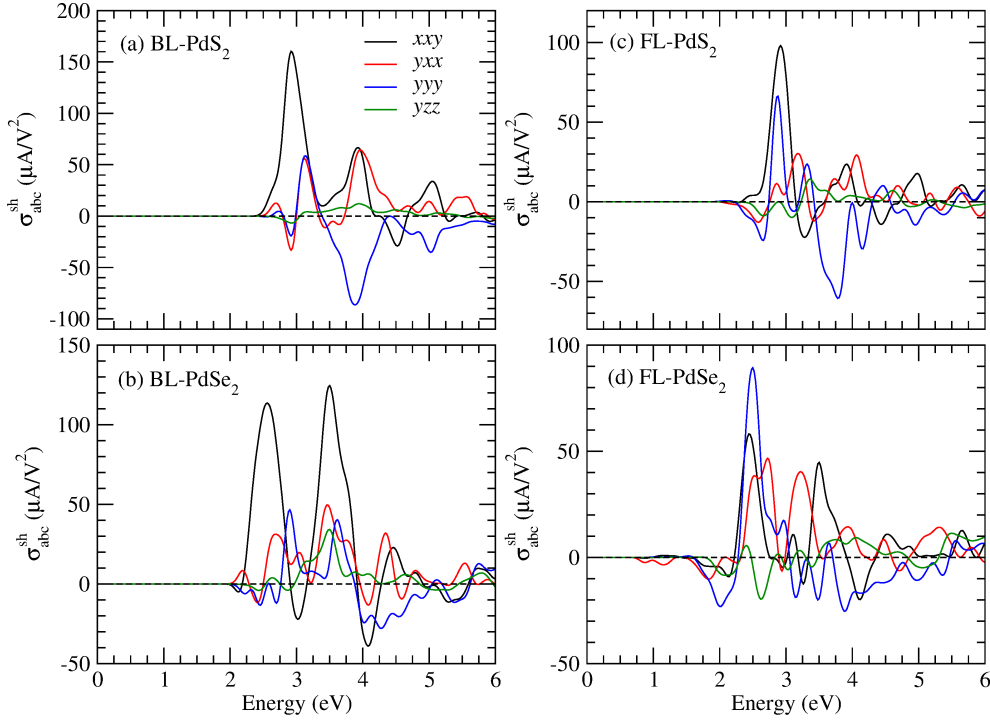


Figure 5: The shift current conductivity of (a) BL PdS<sub>2</sub>, (b) BL PdSe<sub>2</sub>, (c) FL PdS<sub>2</sub> and (d) FL PdSe<sub>2</sub>.

opto-electronic devices. The theoretically predicted shift current conductivity for the archetypal ferroelectrics PbTiO<sub>3</sub> and BaTiO<sub>3</sub> [38], have a value within 10  $\mu A/V^2$  in the visible frequency range, which is in agreement with the earlier experiments [39]. These values are several times smaller than the present predictions for the 2D PdX<sub>2</sub> materials, as shown in Fig. 7(a). Recently, the shift current conductivity of some chiral materials was predicted to be rather large, being in the range of 20~80  $\mu A/V^2$  in the visible frequency range [40]. Furthermore, ML group-IV monochalcogenides were found to exhibit large shift current conductivity of about 100  $\mu A/V^2$  in the visible frequency range. Nevertheless, these values are smaller or at best comparable to the present predictions for the 2D PdX<sub>2</sub> structures (see Fig. 7). Interestingly, the calculated injection current susceptibility of the present PdX<sub>2</sub> structures is two-orders larger than the experimental values of  $1.5 \times 10^8$  A/V<sup>2</sup>s and  $4 \times 10^8$  A/V<sup>2</sup>s for semiconductors CdSe and CdS [41], respectively, which are in the same order of magnitude with the theoretical predictions reported in Ref. [29]. Among the 2D materials, as Fig. 7(b) shows, the injection current susceptibility of ML group-IV chalcogenides was reported to be one-order larger compared to the present PdX<sub>2</sub> structures [46, 49].

### 3.4. Second-harmonic generation

For a noncentrosymmetric material, the nonzero elements of its SHG susceptibility tensor are the same as that of its shift current conductivity tensor. Therefore, as

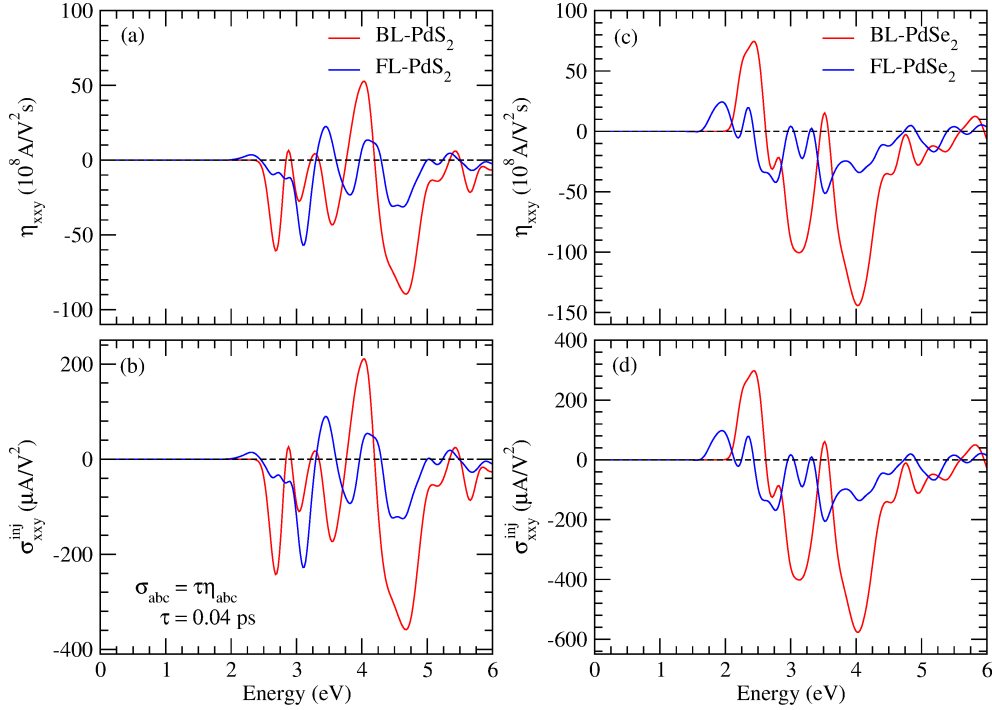


Figure 6: (a) [(c)] Injection current susceptibility ( $\eta_{\xi\xi\xi}$ ) tensor and (b) [(d)] injection conductivity ( $\sigma_{\xi\xi\xi}$ ) of BL and FL PdS<sub>2</sub> [PdSe<sub>2</sub>].

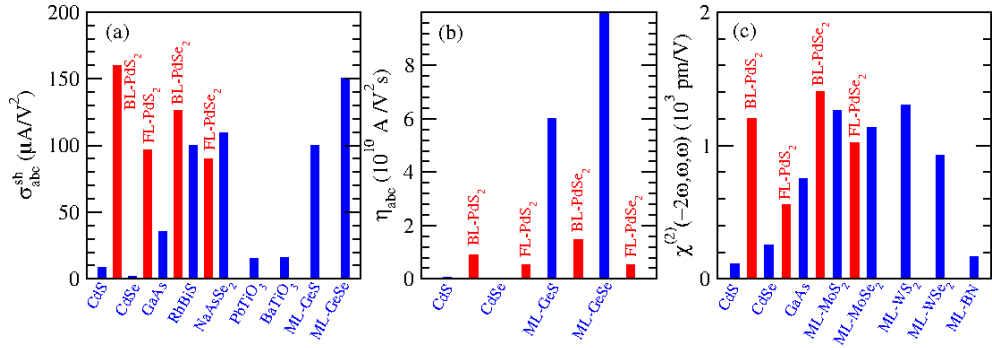


Figure 7: Comparison of maximum nonlinear optical responses of the considered PdX<sub>2</sub> structures with other reported NLO materials within the visible frequency range (i.e., up to 4.0 eV): (a) Shift current conductivity [38, 40–45], (b) injection current susceptibility [41, 44, 46] and (c) SHG susceptibility [5, 47, 48].

for the shift current conductivity, the SHG susceptibility tensor of the BL and FL PdX<sub>2</sub> has five independent nonzero elements, i.e.,  $\chi_{\xi\xi\xi}^{(2)} = \chi_{\xi y \xi}^{(2)} = \chi_{y \xi \xi}^{(2)} = \chi_{\xi y y}^{(2)} = \chi_{y \xi y}^{(2)}$  and  $\chi_{z y z}^{(2)} = \chi_{z z y}^{(2)}$  [3, 4]. The real and imaginary parts as well as the modulus of these nonzero elements for BL PdX<sub>2</sub> and FL PdX<sub>2</sub> are presented in Fig. 8 and Fig. 9,

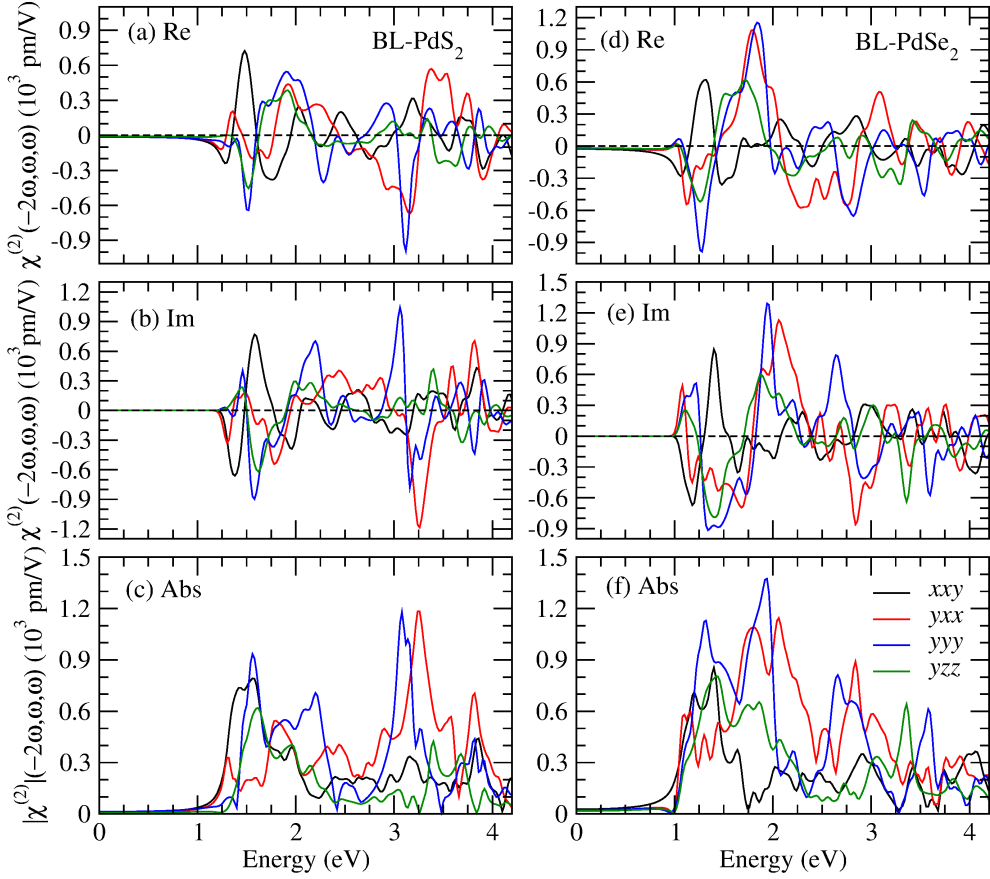


Figure 8: Real (upper panels) and imaginary (middle panels) parts as well as modulus (lower panels) of the SHG susceptibility of BL PdS<sub>2</sub> and BL PdSe<sub>2</sub>.

respectively. Figures 8 and Fig. 9 show that the imaginary (absorptive) parts of the SHG susceptibility for both BL and FL PdX<sub>2</sub> are zero for photon energy being smaller than half of the band gaps but they increase rapidly above half of the band gaps. Furthermore, below half of the band gaps, the real (dispersive) parts of the SHG susceptibility are small and remain almost constant. These nonzero dispersive parts of the SHG susceptibility below half of the band gaps give rise to the low-frequency LEO effect in the PdX<sub>2</sub> structures, which will be discussed in the next section. As for the imaginary parts, they increase rapidly above half of the band gaps.

Among the nonzero SHG susceptibility elements,  $\chi_{yxx}^{(2)}$  and  $\chi_{yyy}^{(2)}$  generally exhibit larger magnitudes in the visible frequency range for all the PdX<sub>2</sub> structures [see Figs. 8(c) and 8(f) as well as 9(c) and 9(f)]. In BL PdS<sub>2</sub>, both  $\chi_{yyy}^{(2)}$  and  $\chi_{yxx}^{(2)}$  spectra show a pronounced peak with almost the same maximum value of  $\sim 1.2 \times 10^3$  pm/V at slightly different photon energies of 3.1 and 3.3 eV, respectively [see Fig. 8(c)]. They come from the negative peak in the real and imaginary parts of the  $\chi_{yyy}^{(2)}$  and  $\chi_{yxx}^{(2)}$  spectra at 3.1 and 3.3 eV, respectively [see Figs. 8(a) and 8(b)]. The  $\chi_{yyy}^{(2)}$  spectrum of BL PdS<sub>2</sub> exhibits the second maximum of  $0.9 \times 10^3$  pm/V at 1.6 eV [see

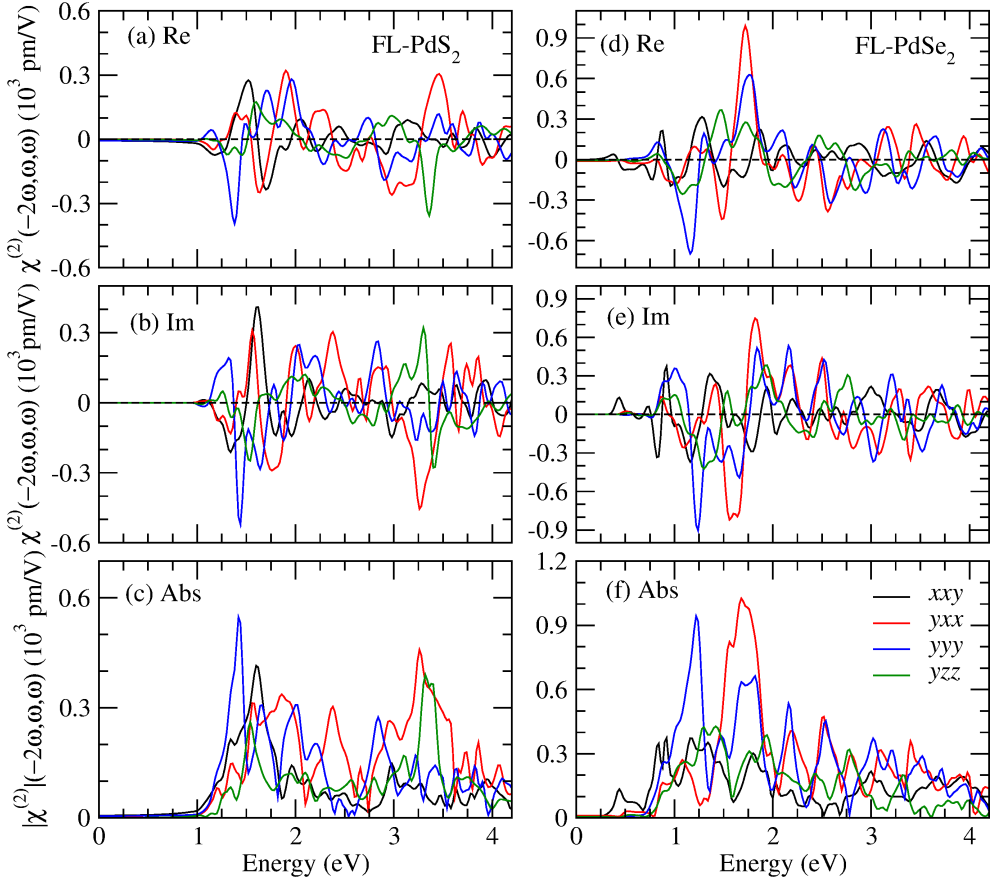


Figure 9: Real (upper panels) and imaginary (middle panels) parts as well as modulus (lower panels) of the SHG susceptibility of FL PdS<sub>2</sub> and FL PdSe<sub>2</sub>.

Fig. 8(c)]. It originates from the negative peak near 1.6 eV in both real and imaginary parts of the  $\chi_{yyy}^{(2)}$  spectrum [see Figs. 8(a) and 8(b)]. Remarkably, the  $\chi_{yyy}^{(2)}$  modulus spectrum of BL PdSe<sub>2</sub> has two gigantic peaks of heights of  $1.1$  and  $1.4 \times 10^3$  pm/V at 1.4 and 1.9 eV, respectively [see Figs. 8(f)] and they stem from the negative and positive peaks at 1.4 and 1.9 eV in the real and imaginary parts of the spectrum [see Figs. 8(d) and 8(e)]. The  $\chi_{yxx}^{(2)}$  spectrum of BL PdSe<sub>2</sub> has a broad twin peak of magnitude of  $1.1 \times 10^3$  pm/V centered at  $\sim 1.9$  eV [see Figs. 8(f)]. Nonetheless, below the band gap, the magnitudes of the  $\chi_{xxy}^{(2)}$  and  $\chi_{yzz}^{(2)}$  spectra of the PdX<sub>2</sub> structures are generally comparable or even larger than that of the  $\chi_{yyy}^{(2)}$  and  $\chi_{yxx}^{(2)}$  spectra. For example, both BL PdS<sub>2</sub> and BL PdSe<sub>2</sub> have a rather broad peak of  $\sim 0.8 \times 10^3$  pm/V at 1.5 and 1.3 eV, respectively [see Figs. 8(c) and 8(f)]. All the  $\chi_{abc}^{(2)}$  spectra from the FL PdX<sub>2</sub> structures are generally smaller than the corresponding spectra of the BL PdX<sub>2</sub> structures. Nonetheless, the magnitudes of the  $\chi_{yyy}^{(2)}$  and  $\chi_{yxx}^{(2)}$  spectra of FL PdSe<sub>2</sub> do peak at 1.2 and 1.7 eV with the large maximum values of  $0.94 \times 10^3$  and  $1.2 \times 10^3$  pm/V, respectively [see Fig. 9(f)].

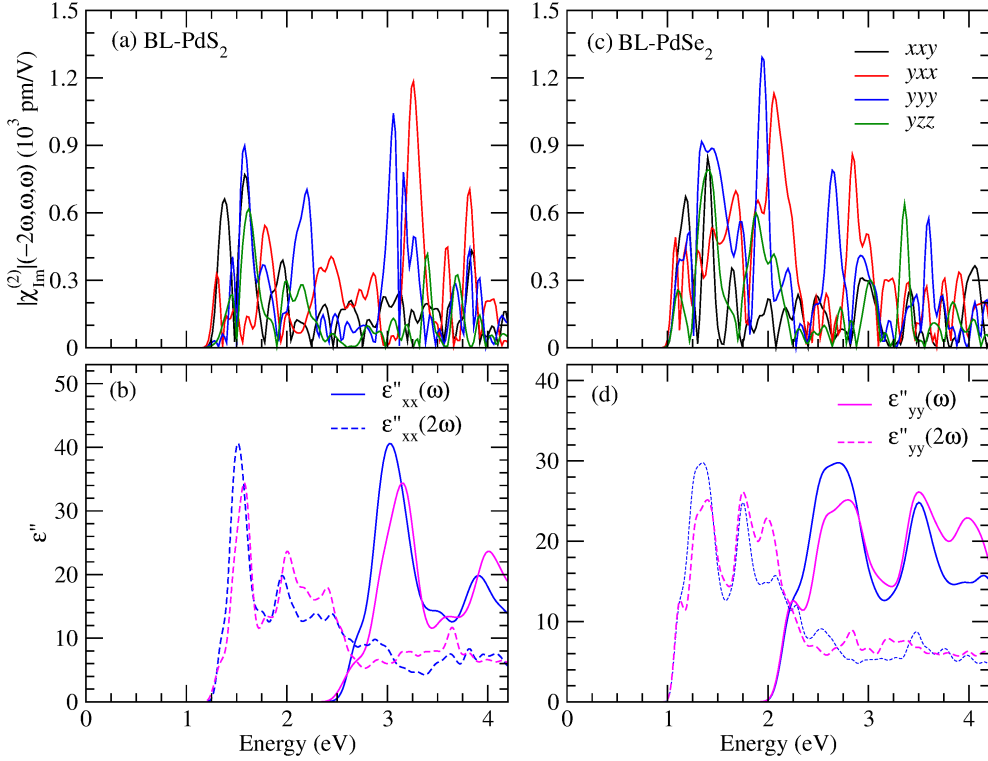


Figure 10: (a)[(c)] Absolute SHG susceptibility and (b)[(d)] imaginary dielectric constant of BL PdS<sub>2</sub> [PdSe<sub>2</sub>].

As shown before (see, e.g., [5] and references therein), the prominent features in the SHG susceptibility are generally caused by either single ( $\omega$ ) and double ( $2\omega$ ) photon resonances or both. This can also be seen from Eqs. (7) and (8). Thus, to help understand the origins of the prominent features in the calculated SHG spectra, we plot the absolute values of the imaginary parts of the nonzero SHG elements of BL PdX<sub>2</sub> and FL PdX<sub>2</sub> in Fig. 10 and Fig. 11, respectively, along with the absorptive parts of the corresponding dielectric functions  $\epsilon''(\omega)$  and  $\epsilon''(2\omega)$ . Figures 10(a) and 10(b) [11(a) and 11(b)] show that the prominent features in the  $|\chi''^{(2)}|$  spectra of BL (FL) PdS<sub>2</sub> in the energy range of 1.2-2.5 eV (1.1-2.2 eV) below the band gap look similar to the features in the  $\epsilon''(2\omega)$  spectra, indicating that they are due to double-photon resonances. Similarly the pronounced features in the  $|\chi''^{(2)}_{yyy}|$  and  $|\chi''^{(2)}_{yxx}|$  spectra above the band gap of 2.5 eV (2.2 eV), have a shape similar to that in the  $\epsilon''(\omega)$ , suggesting that they are caused primarily by single-photon resonances. On the other hand, the  $|\chi''^{(2)}_{yyy}|$  and  $|\chi''^{(2)}_{yxx}|$  spectra above the band gap of 2.5 eV (2.2 eV) have a much reduced amplitude and also are rather oscillatory, being rather similar to the  $\epsilon''(2\omega)$  spectra in this regime. This indicates that they stem mainly from the double ( $2\omega$ ) photon resonances.

We now compare the calculated SHG susceptibility of BL and FL PdX<sub>2</sub> with that reported for other NLO materials. Monolayer group 6B TMDC semiconductors such as MoS<sub>2</sub>, are considered to be the most promising 2D NLO materials because of

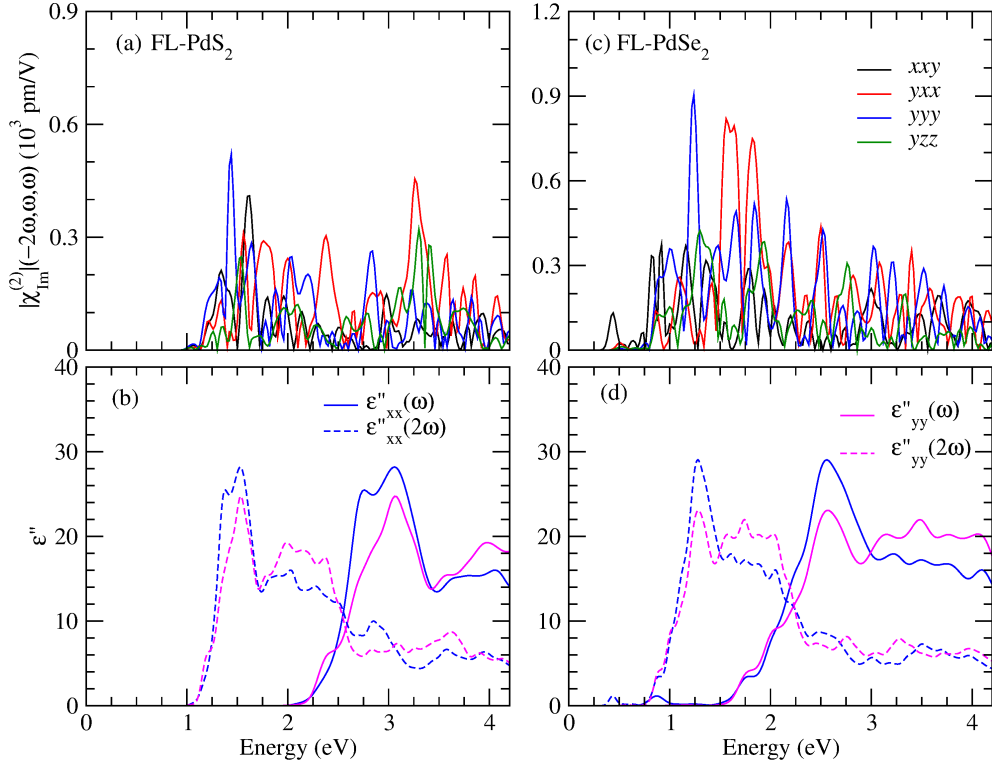


Figure 11: (a)[(c)] Absolute SHG susceptibility and (b)[(d)] imaginary dielectric constant of FL PdS<sub>2</sub> [PdSe<sub>2</sub>].

Table 2: Calculated static dielectric constants ( $\epsilon_x$ ,  $\epsilon_y$  and  $\epsilon_z$ ), second-order optical susceptibility  $\chi^{(2)}(0)$  in pm/V, and linear electro-optical coefficients  $r_{abc}$  in pm/V of BL and FL PdX<sub>2</sub> structures.

	$\epsilon_x$	$\epsilon_y$	$\epsilon_z$	$xyx$	$yxx$	$yyy$	$yyz$
BL-PdS <sub>2</sub>	12.95	12.73	5.97				
$\chi^{(2)}(0)$ (pm/V)				-11	-8.80	-13	-7.04
$r_{abc}$ (pm/V)				0.13	0.11	0.16	0.09
BL-PdSe <sub>2</sub>	13.84	13.90	6.68				
$\chi^{(2)}(0)$ (pm/V)				-28	-22	-24	-18
$r_{abc}$ (pm/V)				0.29	0.23	0.25	0.19
FL-PdS <sub>2</sub>	12.09	11.92	5.40				
$\chi^{(2)}(0)$ (pm/V)				-6.75	1.39	-5.41	-0.42
$r_{abc}$ (pm/V)				0.09	-0.02	0.08	0.01
FL-PdSe <sub>2</sub>	14.84	14.64	8.46				
$\chi^{(2)}(0)$ (pm/V)				-0.96	-12	-4.90	-5.78
$r_{abc}$ (pm/V)				0.01	0.11	0.05	0.05

their direct band gaps and large SHG susceptibility (see [5] and references therein). Remarkably, Fig. 7(c) shows that the maximum values of the SHG susceptibility of BL PdX<sub>2</sub> are comparable or even larger than that of ML group 6B TMDCs [5]. Similarly, FL PdX<sub>2</sub> generally have the SHG susceptibility that are comparable or even larger than that of TL group 6B TMDCs [5]. Interestingly, ReS<sub>2</sub> is another rare TMDC that exhibits second-order NLO responses only when the number of layers is even. The measured SHG susceptibility of BL ReS<sub>2</sub> is large, being about 900 pm/V at 0.8 eV [50]. Nevertheless, this is smaller than that of BL PdS<sub>2</sub> and BL PdSe<sub>2</sub>.

### 3.5. Linear electro-optical coefficient

Here we estimate the LEO coefficients of BL and FL PdX<sub>2</sub> structures, based on the obtained SHG susceptibility at low-frequency limit and static dielectric constant. Note that the LEO coefficients we present here represent only the electronic contribution. There are other contributions to the LEO coefficient such as ionic and piezoelectric contributions, which are beyond of the scope of the present work [53]. The calculated LEO coefficients  $r_{abc}(0)$  at zero frequency along with the static dielectric constants and SHG susceptibilities  $\chi_{xyz}^{(2)}(0,0,0)$  are listed in Table 2. It is clear from Table 2 that BL PdS<sub>2</sub> and BL PdSe<sub>2</sub> have much larger LEO values than FL PdS<sub>2</sub> and FL PdSe<sub>2</sub>. BL PdS<sub>2</sub> and BL PdSe<sub>2</sub> also exhibit a rather strong anisotropy in the LEO effect. Semiconductor GaAs was reported to have a LEO coefficient of  $r_{xyz}(0) = -1.5$  pm/V [54]. Recent calculations [5] predicted that the magnitudes of the LEO coefficients of monolayer group 6B TMDC semiconductors are about 1.5 pm/V, being close to that of GaAs. Table 2 indicates that the LEO coefficients for BL PdS<sub>2</sub> and BL PdSe<sub>2</sub> are many times smaller than that of GaAs [54] and also monolayer group 6B TMDC semiconductors [5]. Nevertheless, they are in the same order of magnitude as that of trilayer group 6B TMDC semiconductors [5].

## 4. Discussion and conclusions

It was recently pointed out [55] that the size of the band gap of a semiconductor is a principal factor that determines the strength of its second-order NLO responses. To understand other origins of the large NLO responses in the 2D PdX<sub>2</sub> structures compared with other NLO materials of similar band gaps, we calculate the deformation charge density, which is defined as the difference between the valence charge density and the superposition of the free atomic charge densities. The calculated deformation charge density distributions for the four 2D PdX<sub>2</sub> structures look very similar. Thus, here we focus only on the deformation charge density of BL PdSe<sub>2</sub>, which is displayed in Fig. 12. Clearly, there is a significant buildup of the electron charge in the vicinity of the Pd-Se bond center by depleting the charge around the Pd atoms along the bond directions. This is caused by the strong directional covalent bonding in BL PdSe<sub>2</sub>, and can lead to an enhanced optical responses due to large spatial overlap between the wavefunctions of the initial and final states, and high anisotropy which would result in large NLO response values [55–57].

In conclusion, we have systematically studied the second-order NLO responses of BL and FL PdX<sub>2</sub> structures using first-principles DFT calculations. First of all, we predict that the BPVE in the considered 2D PdX<sub>2</sub> structures is generally strong, with a large shift current conductivity of up to 130  $\mu\text{A}/\text{V}^2$  and injection current susceptibility of up to  $100 \times 10^8$  A/V<sup>2</sup>s in the visible frequency range. Secondly, we

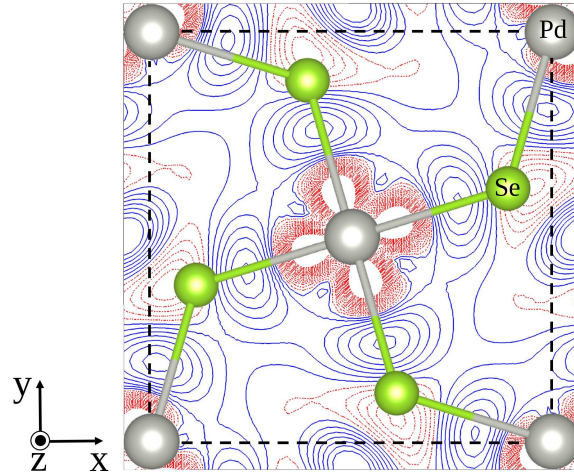


Figure 12: Contour plot of the deformation charge density distribution of BL PdSe<sub>2</sub>. The contour interval is 0.002 e/Å<sup>3</sup>. The electron accumulation is depicted by positive contours (blue solid lines), while the electron depletion is represented by negative contours (red dashed lines). The black dashed line indicates the 2D unit cell [see Fig. 1(c)].

find that all PdX<sub>2</sub> structures possess large SHG susceptibility  $\chi^{(2)}$  in the visible frequency spectrum and BL PdSe<sub>2</sub> has the largest  $\chi^{(2)}$  value of  $1.4 \times 10^3$  pm/V at 1.9 eV. Thirdly, we find that the LEO coefficients of BL PdS<sub>2</sub> and BL PdSe<sub>2</sub> are significant. These superior NLO responses of the BL and FL PdX<sub>2</sub> structures will make them valuable for technological applications in NLO and electro-optic devices such as light signal modulators, frequency converters, electro-optical switches, photovoltaics and photodetector applications. Finally, the strong NLO responses of BL and FL structures of PdX<sub>2</sub> are attributed to strong intralayer directional covalent bonding and also 2D quantum confinement.

**Acknowledgement:** The authors acknowledge the support by the Ministry of Science and Technology and National Center for Theoretical Sciences, Taiwan. The authors also thanks National Center for High-performance Computing, Taiwan for the computing time.

### References

- [1] Mak K F, Lee C, Hone J, Shan J, Heinz T F 2010 *Phys. Rev. Lett.* **105** 136805.
- [2] Radisavljevic B, Radenovic A, Brivio J, Giacometti V, Kis A, 2011 *Nature Nanotechnology* **6** 147.
- [3] Shen Y R 2003 *The Principle of Nonlinear Optics* (John Wiley and Sons Inc., New Jersey, 2003).
- [4] Boyd R W 2003 *Nonlinear Optics* (Elsevier Science, Amsterdam, 2003).
- [5] Wang C -Y and Guo G -Y 2015 *J. Phys. Chem. C* **119** 13268.
- [6] Sturman B I and Fridkin V M 1992 *The Photovoltaic and Photorefractive Effects in Non-Centrosymmetric Materials* (Gordon and Breach Science Publishers, Philadelphia).
- [7] Oyedele, A D, Yang S Z, Liang L B, Puretzky A A, Wang K, Zhang J J, Yu P, Pudasaini P R, Ghosh A W, Liu Z, Rouleau C M, Sumpter B G, Chisholm M F, Rack P D and Geohagan D B 2017 *J. Am. Chem. Soc.* **139** 14090.
- [8] Chow W L, Yu P, Liu F C, Hong J H, Wang X L, Zeng Q S, Hsu C H, Zhu C, Zhou J D, Wang X W et al. 2017 *Adv. Mater.* **29**, 1602969.

- [9] Li E, Wang D, Fan P, Zhang R, Zhang Y -Y, Li G, Mao J, Wang Y, Lin X, Du X and Gao H -J 2018 *Nano Res.* **11** 5858.
- [10] Pi L, Li L, Liu K, Zhang Q, Li H and Zhai T 2019 *Adv. Funct. Mater.* **29** 1904932.
- [11] Lan Y -S, Chen X -R, Hu C -E, Cheng Y and Chen Q -F 2019 *J. Mater. Chem. A* **7** 11134.
- [12] Liang Q, Wang Q, Zhang Q, Wei Q, Lim S X, Zhu R, Hu J, Wei W, Lee C, Sow C, Zhang W and Wee A T S 2019 *Adv. Mater.* **31** 1807609.
- [13] Gronvold F and Rost E 1957 *Acta Cryst.* **10** 329.
- [14] Soulard C, Rocquefelte X, Petit P -E, Evain M, Jobic S, Iti J -P, Munsch P, Koo H -J and Whangbo M -H 2004 *Inorg. Chem.* **43** 1943.
- [15] Kuklin A V and Agren H 2019 *Phys. Rev. B* **99** 245114.
- [16] Puretzy A A, Oyedele A D, Xiao K, Haglund A V, Sumpter B G, Mandrus D, Geohegan D B and Liang L 2018 *2D Mater.* **5** 035016.
- [17] Wu Q and Zhang X-C 1996 *Appl. Phys. Lett.* **68**, 1604.
- [18] Sipe J E and Shkrebtii A I 2000 *Phys. Rev. B* **61** 5337.
- [19] Ahn J, Guo G -Y and Nagaosa N 2020 *Phys. Rev. X* **10** 041041.
- [20] Gudelli V K and Guo G -Y 2020 *Chin. J. Phys.* **68** 896.
- [21] Sun M, Chou J-P, Shi L, Gao J, Hu A, Tang W and Zhang G 2018 *ACS Omega* **3** 5971.
- [22] Kresse G and Joubert D 1999 *Phys. Rev. B* **59** 1758.
- [23] Kresse G and Furthmüller J 1996 *Phys. Rev. B* **54** 11169.
- [24] Kresse G and Furthmüller J 1996 *Comput. Mat. Sci* **6** 15.
- [25] Perdew J P, Burke K and Ernzerhof M 1996 *Phys. Rev. Lett.* **77** 3865.
- [26] Guo G -Y, Chu K C, Wang D -S and Duan C -G 2004 *Phys. Rev. B* **69** 205416.
- [27] Guo G -Y and Lin J C 2005 *Phys. Rev. B* **71** 165402.
- [28] Adolph B, Furthmüller J and Bechstedt F 2001 *Phys. Rev. B* **63** 125108.
- [29] Nastos F and Sipe J E 2010 *Phys. Rev. B* **82** 235204.
- [30] Guo G -Y and Lin J C 2005 *Phys. Rev. B* **72** 075416; 2008 *Phys. Rev. B* **77** 049901.
- [31] Levine Z H and Allan D C 1991 *Phys. Rev. B* **43** 4187.
- [32] Guo G Y and Liang W Y 1986 *J. Phys. C: Solid State Phys.* **19** 5365.
- [33] Heyd J, Scuseria G E and Ernzerhof M 2003 *J. Chem. Phys.* **118** 8207.
- [34] Heyd J, Scuseria G E and Ernzerhof M 2006 *J. Chem. Phys.* **124** 219906.
- [35] Albrecht S, Reining L, Sole R D and Onida G 1998 *Phys. Rev. Lett.* **80** 4510.
- [36] Cai T-Y, Liu S-C, Ju S, Liu C-Y and Guo G-Y 2017 *Phys. Rev. Appl.* **8** 034034.
- [37] Gallego S V, Etxebarria J, Elcoro L, Tasci E S, Perez-Mato J M 2019 *Acta Cryst. A* **75** 438.
- [38] Young S M and Rappe A M 2012 *Phys. Rev. Lett.* **109** 116601.
- [39] Koch W T H, Munser R, Ruppel W and Wurfel P 1976 *Ferroelectrics* **13** 305.
- [40] Zhang Y, de Juan Y, Grushin A G, Felser C and Sun Y 2019 *Phys. Rev. B* **100** 245206.
- [41] Laman N, Bieler M and van Driel H M 2005 *J. Appl. Phys.* **98** 103507.
- [42] Rangel T, Fregoso B M, Mendoza B S, Morimoto T, Moore J E and Neaton J B 2017 *Phys. Rev. Lett.* **119** 067402.
- [43] Brehm J A, Young S M, Zheng F and Rappe A M 2014 *Journal of Chemical Physics* **141**.
- [44] Nastos F and Sipe J E 2006 *Phys. Rev. B* **74** 035201.
- [45] Ibanez-Azpiroz J, Tsirkin S S and Souza I 2018 *Phys. Rev. B* **97** 245143.
- [46] Panday S R, Barraza-Lopez S, Rangel T and Fregoso B M 2019 *Phys. Rev. B* **100** 195305.
- [47] Huang M-Z and Ching W Y 1993 *Phys. Rev. B* **47** 9464.
- [48] Bergfeld S and Daum W 2003 *Phys. Rev. Lett.* **90** 036801.
- [49] Wang H and Xiaofeng Qian X F 2019 *Sci. Adv.* **5** eaav9743.
- [50] Song Y, Hu S, Lin M -L, Gan X, Tan P -H and Zhao J 2018 *ACS Photonics* **5** 3485.
- [51] Zhou X, Cheng J, Zhou Y, Cao T, Hong H, Liao Z, Wu S, Peng H, Liu K and Yu D 2015 *J. Am. Chem. Soc.* **137** 7994.
- [52] Hu L and Huang X 2017 *RSC Adv.* **7** 55034.
- [53] Veithen Jr, Gonze X and Ghosez P 2005 *Phys. Rev. B* **71** 125107.
- [54] Johnston Jr W P and Kaminow I P 1969 *Phys. Rev.* **188** 1209.
- [55] Cheng M, Wu S, Zhu Z Z and Guo G -Y 2019 *Phys. Rev. B* **100**, 035202.
- [56] Song J -H, Freeman A J, Bera T K, Chung I and Kanatzidis M G 2009 *Phys. Rev. B* **79** 245203.
- [57] Ingers J, Maschke K and Proennecke S 1988 *Phys. Rev. B* **37** 6105.

# Large bulk photovoltaic effect and second-harmonic generation in few-layer pentagonal semiconductors PdS<sub>2</sub> and PdSe<sub>2</sub>

Vijay Kumar Gudelli<sup>1</sup> and Guang-Yu Guo<sup>2,1</sup>

<sup>1</sup> Physics Division, National Center for Theoretical Sciences, Taipei 10617, Taiwan

<sup>2</sup> Department of Physics and Center for Theoretical Physics, National Taiwan University, Taipei 10617, Taiwan

E-mail: gyguo@phys.ntu.edu.tw

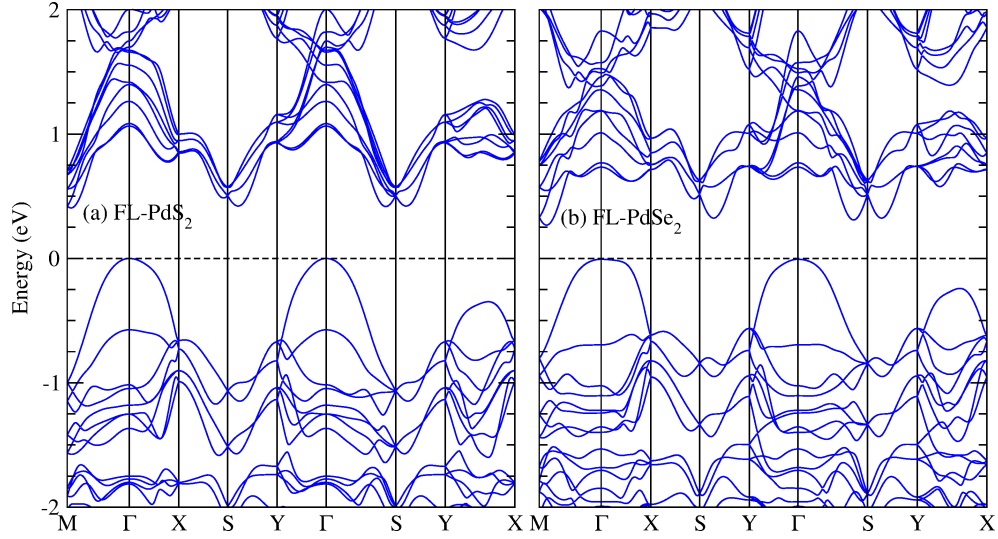


Fig. S1: GGA-functional band structures of (a) FL PdS<sub>2</sub> and (b) FL PdSe<sub>2</sub>. The horizontal black dashed line denotes the top of valence bands.

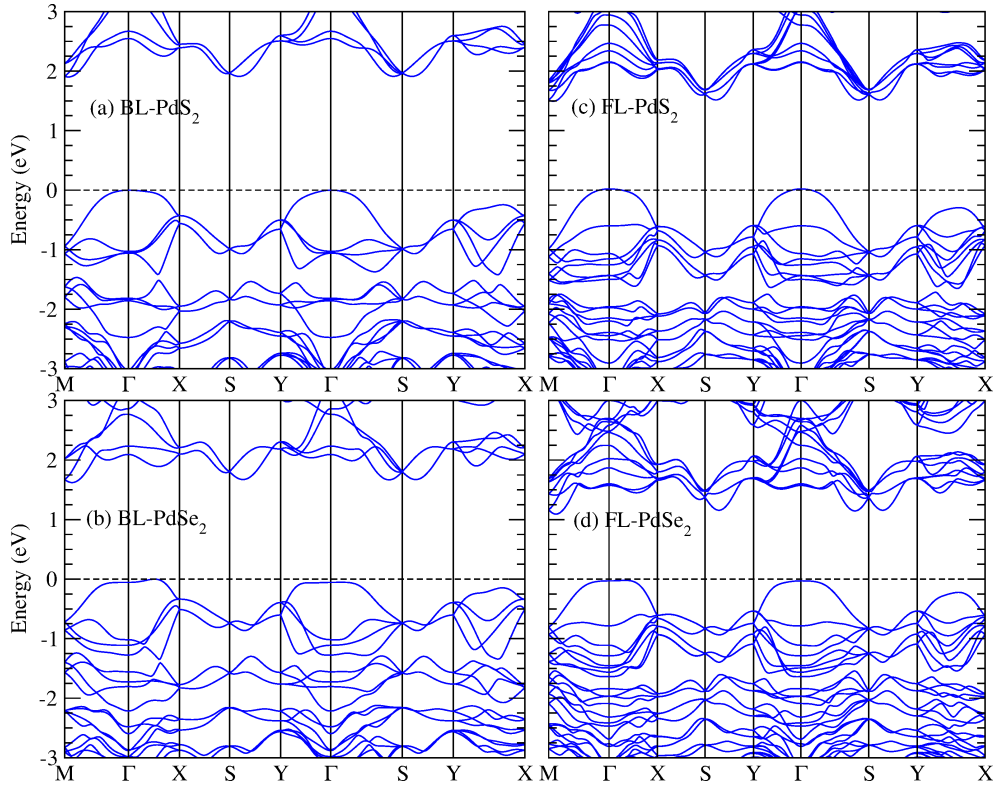


Fig. S2: HSE-functional band structures of (a) BL and (c) FL  $\text{PdS}_2$  as well as (b) BL and (d) FL  $\text{PdSe}_2$ . The horizontal black dashed line denotes the top of valence bands.

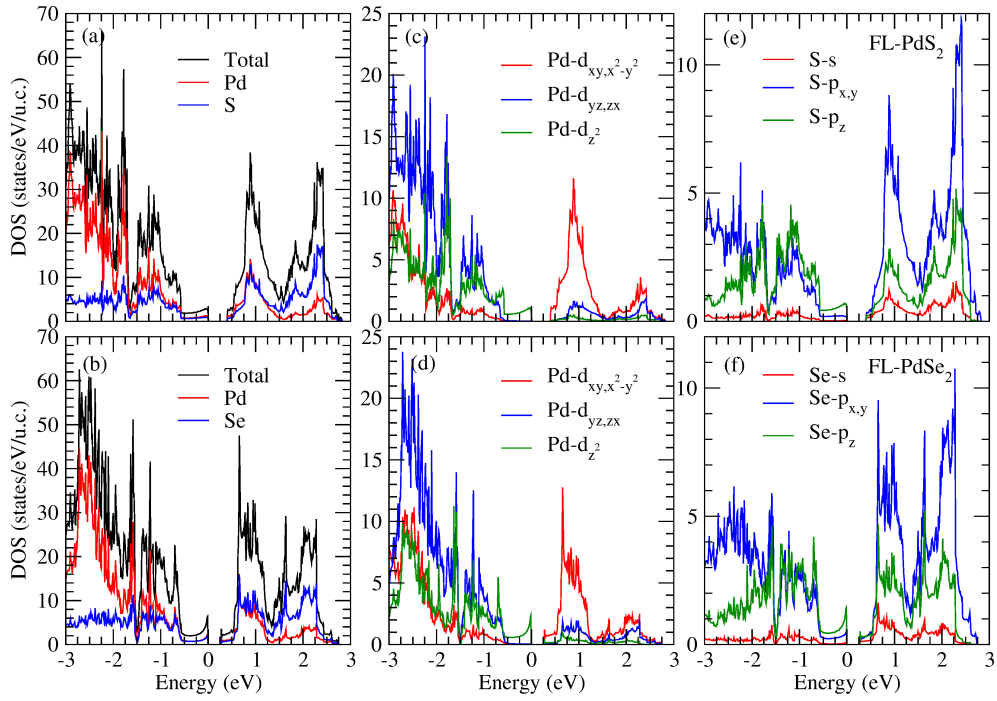


Fig. S3: Total- and orbital-projected densities of states (DOS) for FL  $\text{PdS}_2$  (upper panels) and FL  $\text{PdSe}_2$  (lower panels) obtained using the GGA-functional.